«ФИЗИКА ЭЛЕМЕНТАРНЫХ ЧАСТИЦ И АТОМНОГО ЯДРА»
1997, ТОМ 28, ВЫП.2

УДК 621.3.038
621.3.038.628
621.3.038.615:621.318.3
621.3.038.615:621.319
621.384.634.5

HEAVY ION INJECTION IN SYNCHROTRONS AND STORAGE RINGS

D.Dinev

Bulgarian Academy of Sciences,
Institute for Nuclear Research and Nuclear Energy, Sofia, Bulgaria

A survey of methods for injection of heavy ions in synchrotrons and storage rings is given. Three main injection methods: stacking in transverse phase space, stacking in longitudinal phase space and ion stripping are described in detail. Combinations of multiturn injection with linear coupling, beam cooling and RF stacking are represented. A lot of examples and original results obtained by the author on the simulation of the injection of the Nuclotron booster are given.

Дан обзор методов инжекции тяжелых ионов в синхротроны и накопительные кольца. Подробно описаны три основных метода инжекции: накопление в поперечном фазовом пространстве, накопление в продольном фазовом пространстве и перезарядка ионов. Представлены комбинации многооборотной инжекции и линейной связи колебаний, многооборотной инжекции и охлаждения пучка и многооборотной инжекции и высокочастотного накопления. Приводится множество примеров и оригинальные результаты, полученные автором, по моделированию инжекции в бустер нуклотрона.

1. INTRODUCTION

The last decades show a growing interest in the investigations with heavy ions. Traditional applications of the heavy ion beams in nuclear structure studies and new elements synthesis have been considerably broaden and now cover research fields from fine atomic and molecular physics to beam crystallization. At the same time the nuclear physics studies have evolved to higher energy including experiments with ultrarelativistic ion beams.

It is a remarkable progress in the accelerator physics and techniques that underlies this development.

The milestones of this progress are: the breakthrough in the ion source technology with the invention of the ECR and EBIS sources, the revolutionized impact of the beam cooling technique (electron, stochastic and laser) and the realization that large proton facilities can be used for ion acceleration after modest upgrade.

If twenty years ago tandems, conventional AVF cyclotrons and heavy ion linacs, were used for ion acceleration, nowadays the field of heavy ion facilities covers: large AVF cyclotrons, including superconducting machines; a large number of accelerator-cooler-storage rings for low and medium energy; superconducting heavy ion linacs; existing proton synchrotrons, converted to ion accelerators with energies above 1 GeV/A; new ion synchrotrons and relativistic ion colliders.

This paper represents a survey devoted to the one of the major steps in heavy ion acceleration process — ion injection.

We will restrict ourselves only to discussion of injection in heavy ion synchrotrons and storage rings.

The goal of any injection is to accumulate high current beams with minimum particle losses, i.e., with high efficiency. The accelerator acceptance should be filled as dense as possible.

Many methods developed for injection of protons are applied also for heavy ion accumulation.

Thus fast (single turn) injection by means of a kicker magnet which is switched on during one revolution is used for injection of heavy ions from booster synchrotrons or in cases when the beam pulse from the ion source is too short (EBIS and laser sources). We will not specially discuss this method here as it is elucidated for example in [1].

The intensity of the heavy ion beams produced by the ion sources, especially in high charge states, are limited and as a rule lower than the intensity of the proton beams.

That is why the methods for multiturn injection are of special importance for the heavy ion storage.

There exist methods for particle stacking in either betatron phase space or synchrotron phase space or simultaneously in both.

The betatron stacking is discussed in chapter 2, including the methods applying beam coupling and beam cooling.

Chapter 3 is devoted to the RF stacking.

Another method for ion accumulation is the charge exchange injection. It is widely used in the proton synchrotrons. Applied for injection of heavy ions this method has a lot of peculiarities which are discussed in detail in chapter 4.

Table 1 and Table 2 summarize data on the injection in some of the heavy ion synchrotrons and storage rings now in operation.

Table 1. Injection in heavy ion synchrotrons

Accelerator	SATURNE 2 LNS Saclay	SIS GSI Darmstadt	Synchrophasotron JINR Dubna	Nuclotron JINR Dubna	AGS BNL Brookhaven
Maximum $B\rho$ [Tm]	12.9	18	28	48.5	95
Injector	RFQ + booster MIMAS	a) UNILAC b) storage ring ESR	linac LU20	linac LU20	1 MeV/A tandem + booster
Injection energy [MeV/A]	12.5	a) 11.4 b) 830	5	5	192
Type of injection	RF stacking in MIMAS single turn in SATURNE	a) multiturn + cooling b) fast, bunch to bucket	single turn	single turn	multiturn + coupling in the booster single turn in AGS

Table 2. Injection in heavy ion cooler storage rings

Ring	MIMAS SATURNE Saclay	CRYRING MSI Stockholm	TSR MPI Heidelberg	COOLER IUCF Indiana	TARN 2 INS Tokyo	CELSIUS TSL Uppsala	ESR GSI Darmstadt	COSY KFA Julich
Maximum Bρ [Tm]	1.0	1.4	1.5	3.6	6.1	7.0	10	12
Injector	EBIS + RFQ	CRYEBIS + RFQ	tandem + linac	cyclotron K=220	cyclotron K=70	cyclotron K=180	a) UNILAC b) SIS	cyclotron K=45
Injector energy [MeV/A]	0.187	0.3	0.5–15	55–220	10–68	45–190	a) 1.4 b) 200–320	11–45
Mass range	1–83	2–208	2–130	1–20	1–14	1–16	20–238	1–20
Type of injection	RF stacking	multiturn + electron cool.	RF stacking + multiturn	stripping	RF stacking + multiturn	stripping	a) RF stacking b) fast, bunch to bucket	stripping

2. MULTITURN INJECTION WITH BETATRON STACKING

The classical method of multiturn injection with accumulation of particles in the transverse (radial) phase plane is widely used in heavy ion synchrotrons and storage rings. Some examples are the synchrotron SIS in Darmstadt [2] and the cooler ring CELSIUS in Stockholm [3].

2.1. Principle of the Betatron Stacking. In the betatron stacking method [4—9] the closed orbit is locally distorted by means of two, three or four bump magnets in a way to pass close to the injection septum, Fig.1a. In the beginning the bump is as big as possible and then it is gradually reduced to zero.

In each time $t \in (0, nT_s)$, T_s being the revolution period and n the number of turns during injection, a portion (slice) of the incoming beam is injected into the accelerator. In general the slice center will have linear x_i and angular x_i' displacements with respect to the closed orbit and the slice will undergo betatron oscillations.

One turn later, the slice will come again at the injection azimuth. However due to the betatron oscillations around the instantaneous closed orbit most of the particles will avoid the septum. This is well seen in the normalized phase plane (x, x^*), $x^* = \beta x' + \alpha x$, where β and α are the Twiss structural functions. In the normalized phase space (x, x^*) the particle trajectories are circles, Fig.1b.

Let us for our explanation of the multiturn injection process take horizontal betatron frequency equal to $Q_x = I + 0.25$, I being any integer. With this value of Q_x the particles of the considered slice after four revolutions will come again to their initial positions, i.e., within the septum. Falling again within the septum the slice would undergo wrong bend and will be lost on the vacuum chamber. Fortunately enough, the closed orbit has been meanwhile displaced towards to the machine center. If the closed orbit moves slowly enough comparing to the period of the betatron oscillations, the particle motion will be adiabatic and the particles will follow the orbit. No additional oscillations will be excited. This is depicted on Fig.1c on which three successive positions of the beam slice and closed orbit are shown. Provided the closed orbit displacement during four revolution periods is large enough, the particles of the slice will avoid the septum horizontally and will be accumulated in the accelerator.

Meanwhile a new portion (slice) of the incoming beam will be injected. The particles of this second slice will have larger amplitudes of the betatron oscillations as the orbit bump is reduced and the injection position is kept unchanged.

The process goes on until the bump height is reduced to zero.

It can be shown that the successive slices (or more precisely what remains from each slice after its multiple cutting by the septum edge) lie on a spiral (Fig.1c). The origin of the spiral is on the simultaneous orbit and at the end of

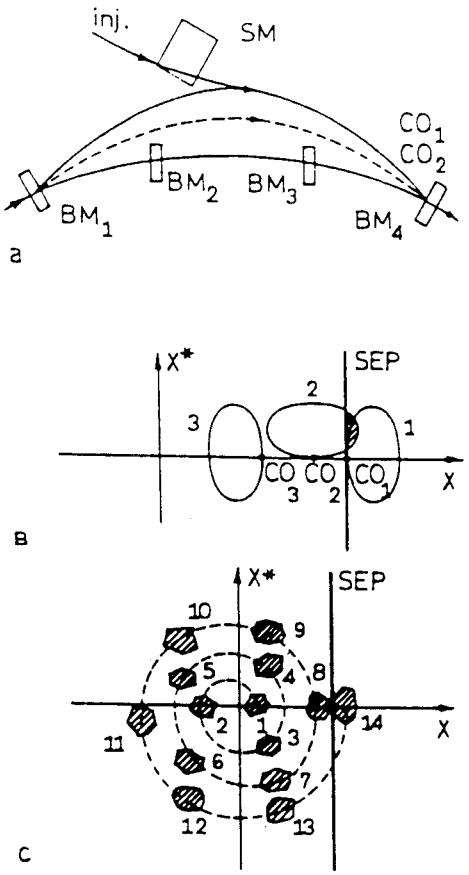

Fig.1. Principle of the betatron stacking: a) closed orbit bump, b) the positions of an injected slice at times t, $t+T_s$, $t+2T_s$. The hatched area will be lost; the fractional part of the Q is taken equal to 0.25. c) the successive positions of the injected beam slices

the injection process it coincides with the machine centre. In the case of linear orbit fall the spiral is Archimed's one.

Computer simulations can describe the stacking process step by step [10,11].

As an example we will use in this paper the project of the booster synchrotron for the superconducting heavy ion synchrotron Nuclotron which is constructed at JINR, Dubna [12]. This will be a six-period synchrotron (Fig.2) with circumference of 50.52 m capable to accelerate protons up to 650 MeV and ions with $Z/A = 0.5$ up to 200 MeV/A. The now in operation linac LU-20 which accelerates protons up to 20 MeV and ions with $Z/A = 0.5$ up to 5 MeV/A will be used as an injector into the booster. The booster will increase the beam intensities in the Nuclotron more than ten times, will raise the final energy of the ions applying ion stripping and will improve beams quality by electron cooling. Other important booster parameters are: beam rigidity at injection 0.647 Tm and maximum 4.3 Tm; betatron tune $Q_h = Q_v = 2.25$; emittance of the injected beam 40 π mm·mrad; acceptance 260 π mm·mrad.

Figures 3 and 4 show the results of the computer simulations. Both the radial (x, x') and the vertical (y, y') transverse phase planes and the transverse cross section (x, y) are shown. On Fig.3 the injection covers three revolution periods (three beam slices are clearly cut in the radial phase plane) while on Fig.4 it covers fifteen periods (the successive slices widely overlap and the density distribution is rather smooth).

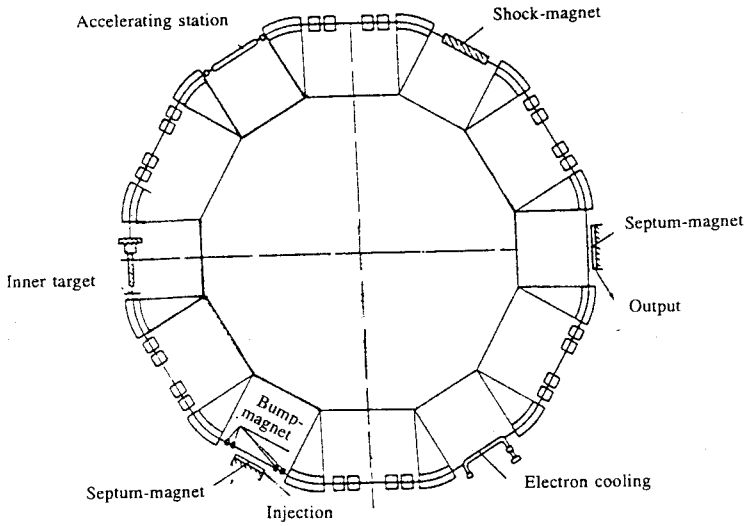

Fig.2. Nuclotron's booster [12]

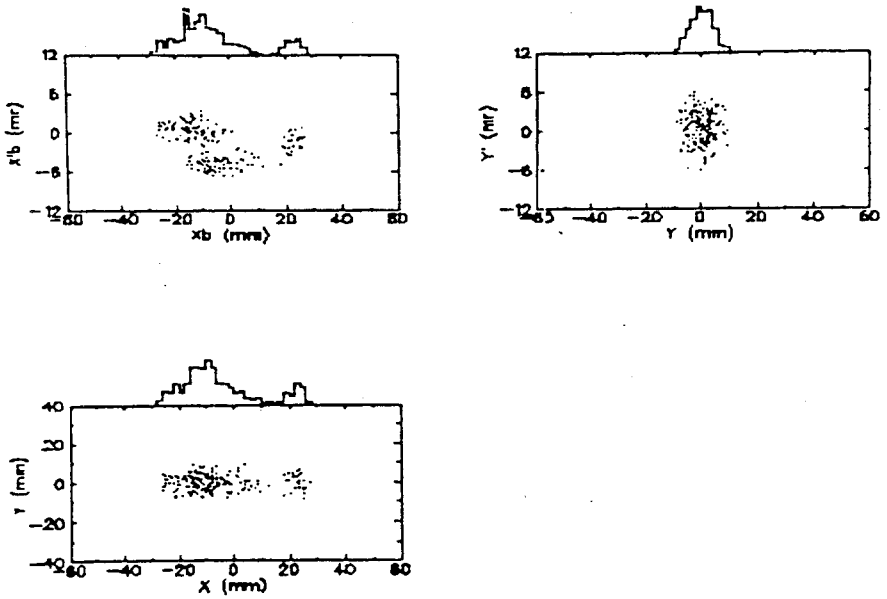

Fig.3. Phase portrait of three-turns injection into Nuclotron's booster [11]

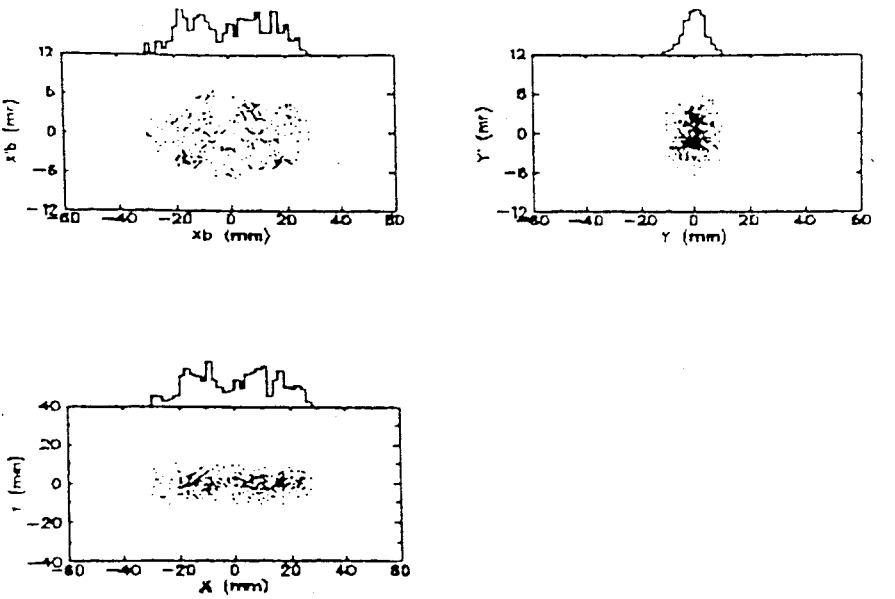

Fig.4. Phase portrait of fifteen-turns injection into the Nuclotron booster [11]

2.2. The Local Orbit Bump. During the *multiturn* injection, a local orbit bump should be produced in order for the beam to pass close to the septum. Let us consider the kicks in the bump magnets necessary for the local closed orbit bump to be produced. Here we will analyse the general case of arbitrary phase distances between the elements given in [13].

A. System with Three Bumpers

A scheme of three bumpers is depicted in Fig.5. The kicks ε_1, ε_2 and ε_9 which produce a closed orbit bump with deviation X_s at the injection azimuth are the solutions of the following system of three equations:

$$\sin \mu_{19} \sqrt{\beta_1}\, \varepsilon_1 + \sin \mu_{29} \sqrt{\beta_2}\, \varepsilon_2 = 0,$$

$$\cos \mu_{19} \sqrt{\beta_1}\, \varepsilon_1 + \cos \mu_{29} \sqrt{\beta_2}\, \varepsilon_2 + \sqrt{\beta_9}\, \varepsilon_9 = 0,$$

$$\sin \mu_{99} \sqrt{\beta_9}\, \varepsilon_9 + \frac{X_9}{\sqrt{\beta_9}}, \qquad (2.2.1)$$

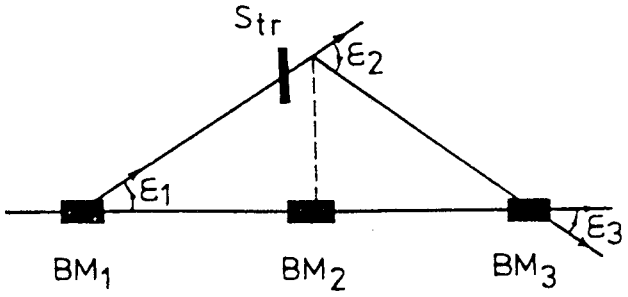

Fig.5. Injection system with three bump magnets

where $\varepsilon_1 = \frac{B_1 l_1}{B\rho}$ is the kick in the first bumper and μ_{12} is the phase advance between BM_1 and BM_2 $\left(\mu_{12} = \int_1^2 \frac{ds}{\beta(s)} \right)$.

B. System with Four Bumpers

Using a system with four bumpers an additional constraint of having a zero slope at injection azimuth can be set, Fig.6. Two cases can be distinguished.

In the first case a drift space is situated between the second and the third bump magnets. Using the Twiss form of transfer matrix, we obtain for the kick in the first bumper:

$$\varepsilon_1 = \frac{X_s}{m_{12}^1} = \frac{X_s}{\sqrt{\beta_1 \beta_2} \sin \mu_{12}}, \tag{2.2.2}$$

where we have denoted by M^1 the transfer matrix from BM_1 to BM_2 and by M^2 the transfer matrix from BM_1 to the septum. The kick in the second bumper should counteract the trajectory slope X':

$$\varepsilon_2 = -X_2' = -m_{22}^1 \varepsilon_1 - \frac{X_s}{\beta_2} (\operatorname{ctg} \mu_{12} - \alpha)_2. \tag{2.2.3}$$

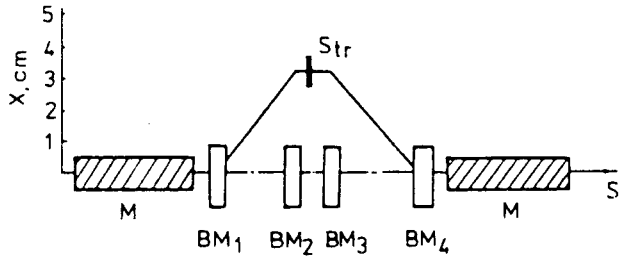

Fig.6. Injection system with four bump magnets

Finally from a symmetry:

$$\varepsilon_3 = -\frac{X_s}{\beta_3}(\mathrm{ctg}\,\mu_{34} - \alpha_3),$$

$$\varepsilon_4 = \frac{X_s}{\sqrt{\beta_3\beta_4}\,\sin\mu_{34}}. \qquad (2.2.4)$$

In the second case when no drift space but some elements (quadrupoles, for instance) lie between the second and the third bumper, it is still possible to obtain a zero slope at the injection azimuth although the trajectory is more complicated.

For the strength of the first two bump magnets one can deduce in this case:

$$X_s = \sqrt{\beta_1\beta_s}\,\frac{\sin\mu_{12}}{(\cos\mu_{2s} - \alpha_s\sin\mu_{2s})}\,\varepsilon_1,$$

$$\varepsilon_2 = -\sqrt{\frac{\beta_1}{\beta_2}}\,\frac{(\cos\mu_{1s} - \alpha_s\sin\mu_{1s})}{(\cos\mu_{2s} - \alpha_s\sin\mu_{2s})}\,\varepsilon_1. \qquad (2.2.5)$$

And from a symmetry:

$$X_s = \sqrt{\beta_s\beta_4}\,\frac{\sin\mu_{34}}{(\cos\mu_{s3} - \alpha_s\sin\mu_{s3})}\,\varepsilon_4,$$

$$\varepsilon_3 = -\sqrt{\frac{\beta_4}{\beta_3}}\,\frac{(\cos\mu_{s4} - \alpha_s\sin\mu_{s4})}{(\cos\mu_{s3} - \alpha_s\sin\mu_{s3})}\,\varepsilon_4. \qquad (2.2.6)$$

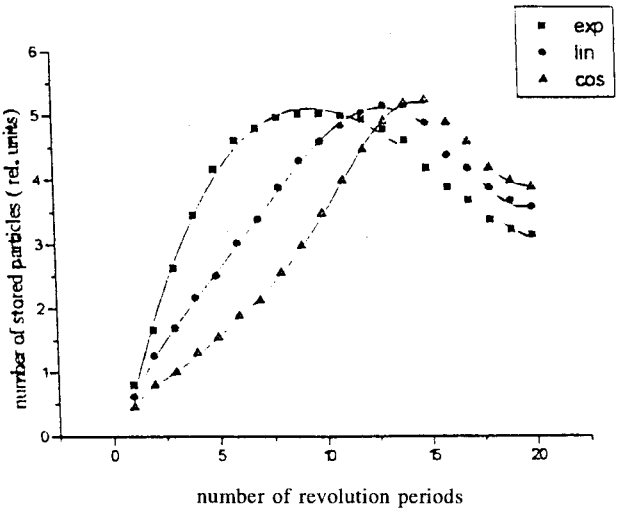

Fig.7. Accumulation of particles in the Nuclotron booster during the multiturn injection for different laws of orbit bump fall [11]. N — number of stored particles, n — number of injection turns. The injection covers fifteen turns

2.3. Stacking Efficiency. The injection efficiency is defined as the ratio of the accumulated beam current to the product of the injector current by the number of injection periods.

Different kinds of orbit bump falls — linear, experimental, cosine, etc., could be applied. If the bump fall is exponential (Fig.7), the number of accumulated particles increases faster while the losses during the last periods are quite big due to the small orbit step. On the contrary the cosine bump fall has bigger losses during the first periods.

The stacking efficiency slightly depends on the bump fall law, Fig.8.

The stacking efficiency depends on large number of parameters: the distance injected beam centre — septum, the slope of the injection beam, the number of injection periods (injection time), the number of betatron oscillations per turn, Q, the injector emittance, the momentum spread in the injected beam, etc.

The efficiency versus the initial radial position of the injected beam X_0 and the efficiency versus the injected beam slope X_0' curves have resonant character, Fig.9 and Fig.10.

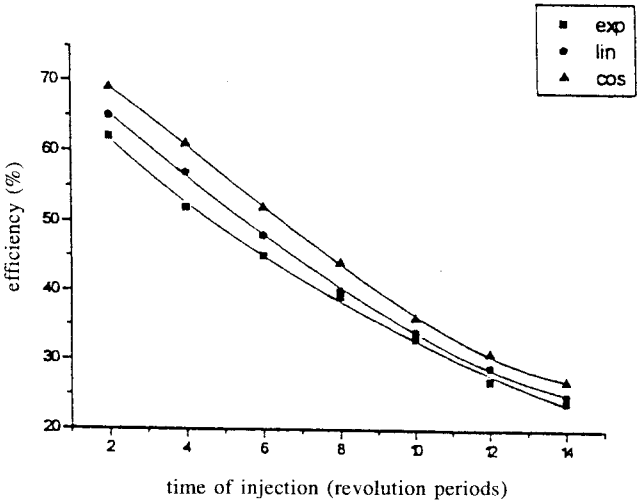

Fig.8. Efficiency in the Nuclotron's booster versus the number of injected turns for different laws of orbit bump fall

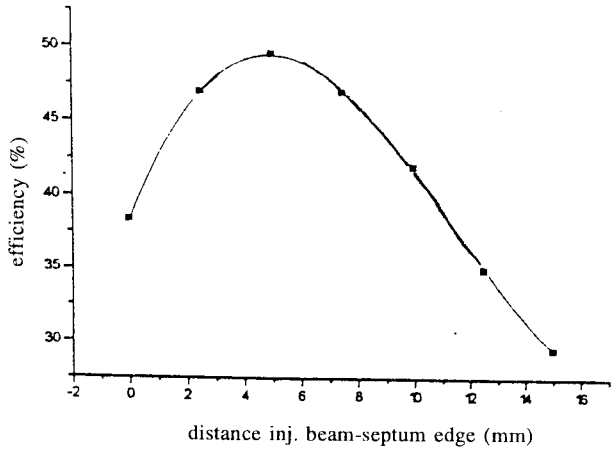

Fig.9. Efficiency in the Nuclotron's booster versus the distance injected beam centre — septum [11]

The dependence of the efficiency on the betatron number Q has a typical symmetrical shape, Fig.11.

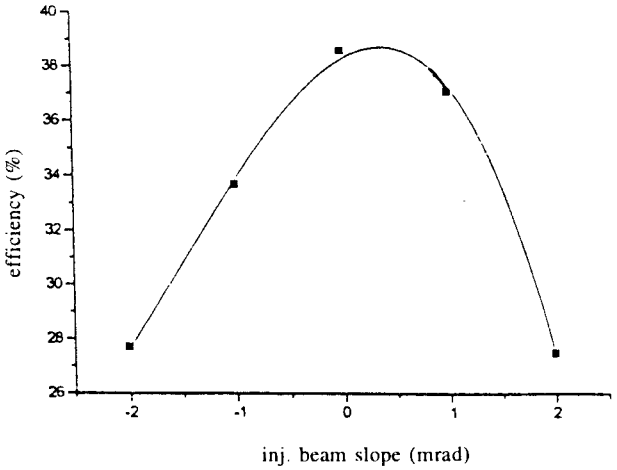

Fig.10. Efficiency in the Nuclotron's booster versus the injected beam slope [11]

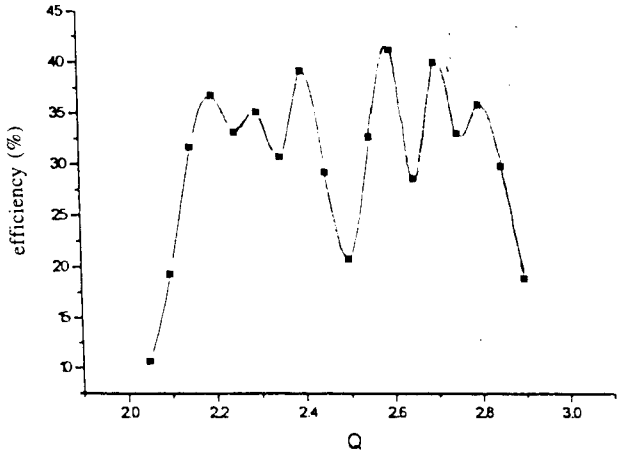

Fig.11. Efficiency in the Nuclotron's booster versus the betatron number Q [11]

2.4. Improvements of the Multiturn Injection with Betatron Stacking. *2.4.1. Multiturn Injection with Linear Coupling.* If both the horizontal and the vertical emittances of the injected beam are sufficiently smaller than the acceptance of the ring, one can realize multiturn injection with stacking in both horizontal and vertical phase spaces applying linear coupling of the betatron oscillations [14, 15].

The linear coupling occurs when $Q_x \approx Q_z$ in the presence of skew quadrupole or solenoidal magnetic fields. The strength of the coupling if excited by skew quadrupole is determined by [16]:

$$C_q = \frac{R}{2\pi Q} \frac{l}{B\rho} \oint \left(\frac{dB_x}{dx} \right)_{z=0} ds. \tag{2.4.1}$$

The linear coupling leads to beating of the horizontal and the vertical betatron oscillations. The amplitudes of the oscillations in smooth approximation are:

$$|X|^2 = |A|^2 + |B|^2\chi^2 - 2|AB^*|\,\chi \cos(Q_c\,\theta),$$

$$|Z|^2 = |B|^2 + |A|^2\chi^2 + 2|AB^*|\,\chi \cos(Q_c\,\theta), \tag{2.4.2}$$

where

$$\chi = \sqrt{1+\xi^2} - \xi, \tag{2.4.3}$$

$$\xi = \frac{B\rho Q \Delta}{R^2 \left\langle \frac{dB_x}{dx} \right\rangle}, \tag{2.4.4}$$

$$\Delta = Q_x - Q_z, \tag{2.4.5}$$

$$Q = \frac{Q_x + Q_z}{2}. \tag{2.4.6}$$

In (2.4.2) A and B are two complex constants of the motion whose values are determined by the initial conditions and Q_c is the beating wave number.

It can be shown that:

$$Q_c = \sqrt{\Delta^2 + C_q^2}. \tag{2.4.7}$$

According to (2.4.2) there exists a sinusoidal exchange of energy from the horizontal to the vertical betatron oscillations and vice versa while the whole energy, i.e., $|X|^2 + |Z|^2$ keeps constant.

Thus a beam injected in the medium plane close to the vacuum chamber wall will undergo horizontal betatron oscillations with decreasing amplitude. The energy of the horizontal oscillators goes to excite vertical betatron oscillators with increasing amplitude. After a half of beating period the beam will be dismissed horizontally towards the machine centre and vertically off the medium plane to the highest degree.

The depth of the amplitude modulation during the beating is given by:

$$S = \frac{C_q}{\Delta^2 + C_q^2}. \tag{2.4.8}$$

After that the process will go back to small vertical and maximum horizontal amplitudes of the oscillations that is why the injection process must be stopped.

As a result we will have phase space painting in both horizontal and vertical planes.

The multiturn injection of heavy ions with linear coupling is realized, for instance, in the AGS booster [17].

The injection is from 1 MeV/u tandem Van de Graaf which delivers ion beams with very small transverse emittance. This allows very efficient multiturn injection (Fig.12). The unperturbated tunes are $Q_x = 4.833$ and $Q_z = 4.780$. A skew quadrupole induces significantly X–Z coupling during the injection. Typically about 40 turns can be injected with efficiency of 65%. Applying this scheme the beam intensity has been increased more than 50%.

2.4.2. Combination of Multiturn Injection with Beam Cooling. If the beam lifetime is long comparing to the cooling time it will be possible to combine at electron cooling at injection energy with betatron stacking.

The cooler voltage is chosen not to change the average ion momentum. During the cooling the beam shrinks transversally and new injection pulses can be put next to the stack in the horizontal phase space. The injection consists in repetitive combinations of multiturn injection and successive electron cooling.

Such kind of injection is realized in the heavy ion synchrotron SIS and in the cooler ring CRYRING.

In SIS the injection covers from 10 to 15 cycles within 1s and allows the accumulation of $4 \cdot 10^9$ particles per pulse [18]. The cooling time for U^{79+} ions with 11.4 MeV/u energy is about 100 ms. The cooling reduces the beam emittance from 100 π mm·mrad down to 30 π mm·mrad. A series of ten

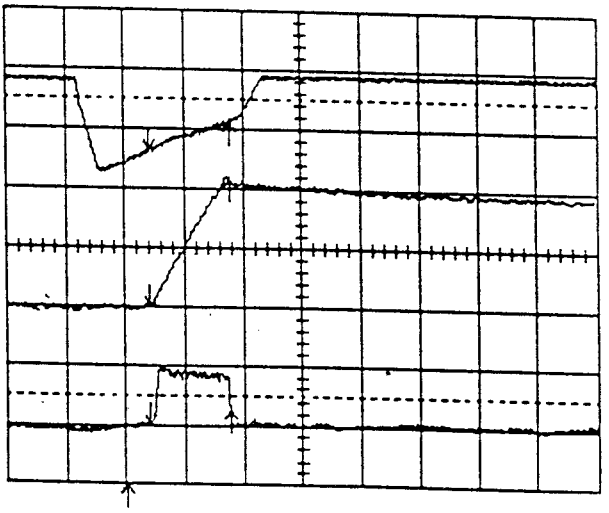

Fig.12. Multiturn injection in the AGS booster. Oscilloscope traces of the injection kicker (top); circulating beam current (middle); beam pulse from the Tandem (bottom). One horizontal box corresponds to 500 μs [17]

repetitive multiturn injections with 80% efficiency will allow accumulation of $4 \cdot 10^9$ ions per pulse.

In CRYRING this combination is applied for the lightest fully stripped ions [19]. Thus the lifetime of deuterons at 290 keV/u is 300 s. Provided the cycle betatron stacking-cooling lasts 3 s it will be possible to improve the stored intensity 100 times. The real efficiency is sufficiently smaller, as the stack of cooled ions occupies a part of the phase space where normally some of the injected pulses go. Nevertheless, 60 μ A ($2 \cdot 10^9 p$) has been stored in the ring.

The accumulated intensity in the stacking-cooling process is limited by the space charge effects (incoherent space charge instabilities).

3. BEAM STACKING WITH RF ACCELERATION

3.1. Principle of the RF Stacking. Storage of the injected particles in the longitudinal phase space was first suggested by Symon and Sessler in MURA [20]. Later this method was experimentally investigated in the model electron

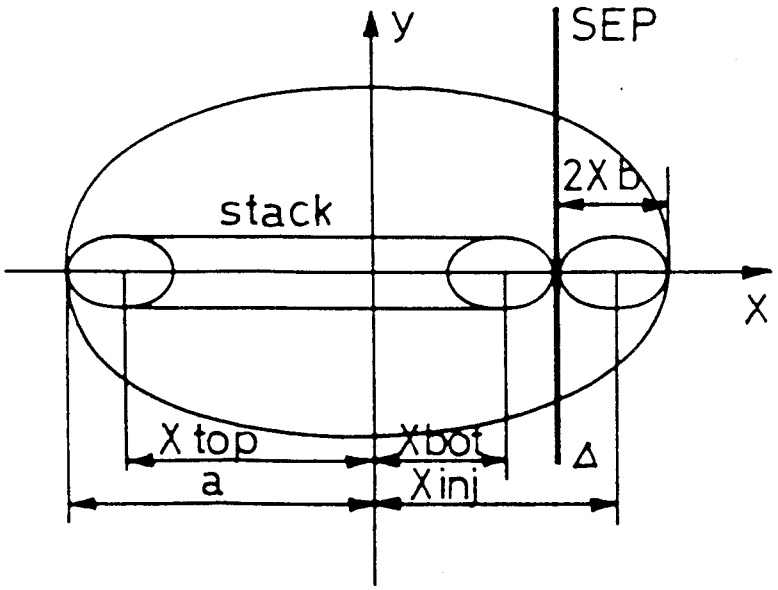

Fig.13. Location of the injected and stacked beams in the accelerator aperture

storage ring CESAR in CERN [21]. The RF stacking was used successfully for many years in the proton storage ring ISR in CERN [22].

The principle of the RF stacking [20–24] can be understood from Fig.13, where a transverse cross section of the accelerator is shown.

The beam is injected by means of an electrostatic septum at position X_{inj}. After the injection of the first portion of particles is completed, the stacking RF cavity is switched on and the particles are accelerated (or more usualy decelerated) to an outer (inner) orbit according to:

$$\frac{E}{R}\frac{dR}{dE}=\frac{\alpha}{\beta^2}, \tag{3.1.1}$$

where R is the physical radius of the machine; β is the relativistic factor and α is the momentum compaction factor [25,26]:

$$\alpha=\frac{p}{R}\frac{dR}{dp}=\frac{\langle D_x\rangle_m}{R}. \tag{3.1.2}$$

In (3.1.2) $\langle\,\rangle_m$ denotes averaging over the dipoles only and D_x is the dispersion.

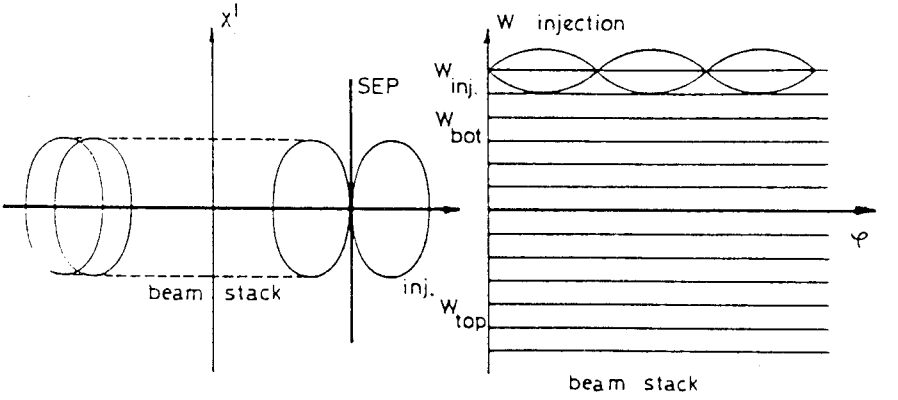

Fig.14. Principle of the RF stacking

When the top of the stack is reached, the RF voltage is abruptly switched off and the particles are released from the RF buckets.

The RF cycle then is repeated and the next injected portion is trapped in buckets and accelerated (decelerated).

There are two modes of operation.

In the so-called «repetitive stacking» mode or «stacking at the top» the new portion is moved again to the same position, i.e., to the top of the stack. According to Liouville's theorem the particle density in the longitudinal phase space must be conserved [26]. Hence the particles already accumulated in the stack will be displaced toward lower (higher) energies. Due to the very small value of the momentum compaction factor (3.1.2) in the strong focusing rings the portions of particles with different energies largely overlap in the physical and transverse phase spaces, Fig.14. The stacking takes place in the longitudinal phase space while the density in the 6-dimensional μ-phase space is conserved in agreement with Liouville's theorem. A beam stack with large intensity is built up.

In the «non-repetitive stacking» mode or «stacking at the bottom» each successive portion of particles is moved to a slightly different energy than the previous one. The energy difference is equal to the final bucket area A_b divided by 2π; so as the new particles will be added to the bottom of the stack.

3.2. Longitudinal Phase Space Topology. As this has been shown first by Symon and Sessler [20], the equations of the longitudinal motion in an accelerator can be put in Hamilton's form with canonically conjugated variables:

$$W = 2\pi \int_{E_0}^{E} \frac{dE}{\omega(E)} \qquad (3.2.1)$$

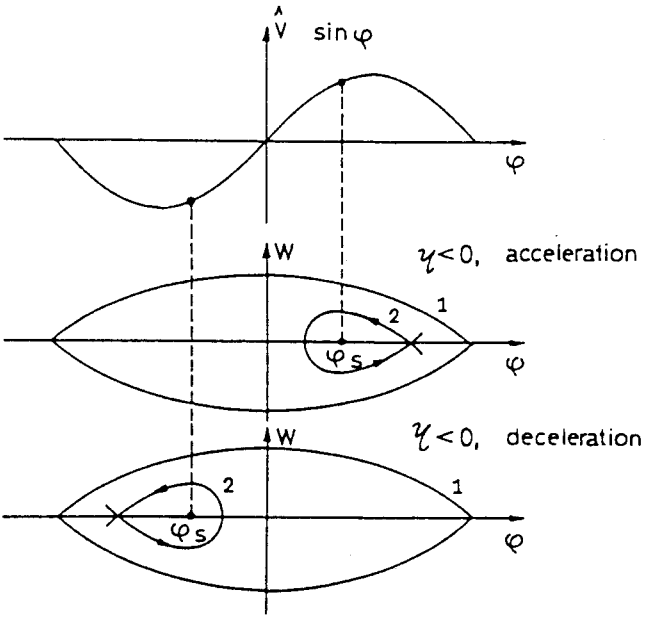

Fig.15. Stationary and moving RF buckets

and the *RF* phase φ. In (3.2.1) ω(*E*) is the revolution frequency of a particle with energy E and E_0 is an arbitrary energy.

The area of stable oscillations around the synchronous particle, the so-called RF bucket is shown on Fig.15 for the stationary case ($\Gamma = \sin\varphi_s = 0$; no acceleration (deceleration)) and for the moving buckets ($\Gamma = \sin\varphi_s \neq 0$; the particles are accelerated (decelerated)).

Let h be the harmonic number of the RF, so as we will have h buckets simultaneously on the accelerator circumference. The area of these h buckets is:

a) for stationary buckets

$$A_{bs} = \frac{8\beta}{\omega_s}\sqrt{\frac{8\pi e\hat{V}E_s}{h|\eta|}}, \tag{3.2.2}$$

b) for moving buckets

$$A_b = A_{bs}\alpha^*(\Gamma). \tag{3.2.3}$$

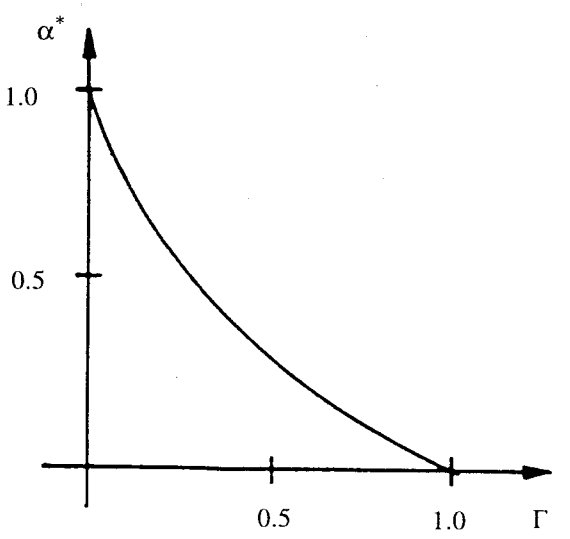

Fig.16. The function $\alpha^*(\Gamma)$

Here

$$\eta = \frac{p}{\omega}\frac{d\omega}{dp} = \frac{1}{\gamma^2} - \alpha = \frac{1}{\gamma^2} - \frac{1}{\gamma_{tr}^2}, \tag{3.2.4}$$

γ — the relativistic factor and γ_{tr} — its value at the transition point. In (3.2.3) $\alpha^*(\Gamma)$ is a tabulated function of the synchronous phase $\Gamma = \sin\varphi_s$ (Fig.16). In the RF stacking an important role is played by the adiabatic theorem of Boltzman–Ehrenfest [26], which states that if the parameters (such as $\hat{V}$, φ_s, E_s, etc.) in the Hamiltonian, H, are varied sufficiently slowly the particles lying on a closed curve $H(t_1) = \text{const}$ surrounding an area of stable oscillations A_1 at a time t_1 will remain on a closed curve $H(t_2) = \text{const}$ surrounding an area $A_2 = A_1$ at a time $t_2 > t_1$. Thus the action integral $I = \oint W d\varphi$ is an invariant.

3.3. Stacking Cycle. It is the phase displacement phenomenon that undelie the Rf stacking process. The phase displacement is a phenomenon related with the crossing of a coasting beam by RF bucket (no matter filled with particles or empty). The trajectories outside the separatrix are such that the particles will

move in the opposite to the bucket direction (for an accelerating bucket to lower energy and for an decelerating bucket to higher energy). According to Liouville's theorem the area of the displacement of the coasting beam must be equal to the bucket area A_b. Hence the change in the mean energy of the coasting beam is:

$$\Delta W = \frac{A_b}{2\pi}. \tag{3.3.1}$$

A detailed calculation of the change of the energy of a particle lying outside a moving bucket when this bucket crosses the particle is made in [27,28]. It shows that the mean energy change follows (3.2.1) while the energy spread in the coasting beam is increased.

Let's now look at the RF stacking cycle in more detail.

The stacking is performed at a constant magnetic field.

After the first portion of particles is injected, it immediately debunches due to the spread in the revolution frequency of particles having different energies.

The RF voltage is now switched on adiabaticaly while the RF frequency is kept constant ($\varphi_s = 0$). The particles are trapped with big efficiency (more than 90%) in stationary buckets.

After the capture finishes, the RF buckets are decelerated toward to the top of the stack.

As:

$$\frac{E}{\omega}\frac{d\omega}{dE} = \frac{\eta}{\beta^2} \tag{3.3.2}$$

and

$$\frac{dE}{dt} = \frac{\omega}{2\pi} e\hat{V} \sin \varphi_s, \tag{3.3.3}$$

the RF frequency must be increased according to:

$$\frac{d\omega_{rf}}{dt} = \frac{\eta\, \omega_{rf}^2}{2\pi\, h\, \beta^2 E} e\hat{V} \sin \varphi_s. \tag{3.3.4}$$

When ω_{rs} reaches the final frequency, the RF voltage is switched off, the bunches debunch and a whole strip in the stack is populated with particles.

In the repetitive stacking mode each of the successive pulses crosses the whole stack and the particles are released at the top of the stack.

In each crossing the already stored particles are moved to higher energy by (3.3.1) according to the phase displacement mechanism.

If the stack is built by n pulses, the ideal stack width will be:

$$2\pi \frac{\Delta E_{\text{ideal}}}{\omega} = n \frac{A_b}{2\pi}. \tag{3.3.5}$$

In fact the particles will be distributed over wider energy range $\Delta E_s > \Delta E_{\text{ideal}}$.

In the non-repetitive stacking mode the crossing of the whole stack by the buckets is avoided by successive reducing of the final RF frequency by:

$$\Delta \omega_{\text{rf}} = \frac{\omega_{\text{rf}}^2 \eta}{\beta^2 E h} \frac{A_b}{(2\pi)^2}. \tag{3.3.6}$$

Thus the particles will be deposited at the stack bottom.

It is natural to define the stacking efficiency as the ratio of the average phase space density in the stack to that in the injected beam [29].

The total stacking efficiency depends on two kinds of parameters:

$$\varepsilon_{\text{tot}} = \varepsilon' \varepsilon. \tag{3.3.7}$$

Here ε' describes the dependence of the stacking efficiency of the RF manipulation — mainly on the trapping efficiency in the buckets.

In (3.3.7) ε is the accumulation efficiency itself:

$$\varepsilon = \frac{N_{\text{lim}}}{N_{\text{tot}}}, \tag{3.3.8}$$

where N_{lim} is the number of particles in the ideal stack width and N_{tot} is the total number of particles in the stack.

Function ε represents the reduction of the phase space density due to the dilution of the stack by the moving RF buckets during the subsequent stacking cycles.

Experiments and computer simulations [29] show that ε is a function of the synchronous phase $\Gamma = \sin \varphi_s$ and of the number of stacking cycles n. There is an empirical formula:

$$\varepsilon = \frac{1}{1 + \dfrac{2\Gamma}{3\sqrt{n}\,\alpha^*(\Gamma)}}, \tag{3.3.9}$$

which agrees quite well with the experimental results over a wide range of Γ and for not too small n.

As $\alpha^*(\Gamma)$ is a decreasing function of φ_s (Fig.15), the stacking efficiency $\varepsilon \to 1$, when $\varphi_s \to 0$.

However small values of φ_s will require very long stacking times according to (3.3.4), i.e., a compromise must be made.

3.4. Combination of Multiturn Injection and RF Stacking. Both the multiturn injection and the RF stacking have their limits in the intensity of the accumulated beams. These limits have been already discussed above.

If we combine both accumulation mechanisms, much larger intensity multiplication factors can be realized. The stacking will take place in the 4-dimensional (x, x', W, φ) phase space. The physical aperture of the accelerator however must be shared by booth the methods. Let ε_0 be the area of the transverse phase plane (x, x') devoted to the multiturn injection. In order to estimate this area a pure geometrical analysis can be carried out [30].

From Fig.13 one can easily deduce that

$$E_{\text{inj}} - E_{\text{top}} \leq 2E\beta^2 \left(\frac{a - \sqrt{\varepsilon_0 \beta(s)}}{D(s)} \right) \tag{3.4.1}$$

must be satisfied for any point s along the circumference, $\beta(s)$ being the Twiss amplitude function; and $D(s)$, the dispersion.

On the other hand, in the injection point:

$$E_{\text{inj}} - E_{\text{bot}} = E\beta^2 \left(\frac{2\sqrt{\varepsilon_0 \beta_{\text{inj}}} + \Delta}{D_{\text{inj}}} \right), \tag{3.4.2}$$

where Δ is the septum thickness.

Let S^* be the azimuth at which the right-hand side of (3.4.1) has a minimum and the corresponding values of $\beta(s)$ and $D(s)$ be β^* and D^*.

The number of RF cycles is:

$$n_{\text{rf}} = \varepsilon_{\text{rf}} \frac{E_{\text{bot}} - E_{\text{top}}}{\Delta E}, \tag{3.4.3}$$

where ΔE is the phase displacement of the stack during a single crossing by the buckets (3.3.1) and ε_{rf} is the stacking efficiency here defined as the ratio of the ideal stack width to the width of the real stack [21].

The number of the effective turns in the multiturn stage of the combined process is:

$$n_m = \varepsilon_m \frac{\varepsilon_0}{\varepsilon_{inj}}, \tag{3.4.4}$$

where ε_{inj} is the emittance of the injected beam, ε_m is the multiturn injection efficiency.

Thus the total number of effective turns will be:

$$n_{tot} = n_m \cdot n_{rf} = \varepsilon_m \varepsilon_{rf} \frac{E\beta^2}{\Delta E} \varepsilon_0 \left[\frac{2(a - \sqrt{\varepsilon_0 \beta^*})}{D^*} - \frac{2\sqrt{\varepsilon_0 \beta_{inj}} + \Delta}{D_{inj}} \right]. \tag{3.4.5}$$

From (3.4.5) the optimum value of the phase area devoted especialy to the multiturn injection can be calculated.

3.5. RF Stacking Examples

A. Heidelberg Test Storage Ring (TSR)

The Heidelberg Heavy Ion Test Storage Ring (TSR) [31] is an experimental accelerator specially designed to investigate the electron cooling of heavy ions and the combined RF stacking scheme as well. The ring is able to store ions with energy up to 30 MeV/A (for $Z/A = 0.5$) accelerated in a MP tandem — postaccelerator combination. The emittance of the injected particles is 1.5 π mm·mrad and the injected current 9 μA.

A combined .scheme of multiturn injection and RF stacking is used [32]. The phase area devoted to betatron stacking is $\varepsilon_0 = 96\ \pi$ mm · mrad. It is filled for about 100 turns with an efficiency of 40%.

The repetitive stacking mode is chosen for the RF stage of the accumulation process. Ther efficiency of the adiabatic capture of the ions in the buckets is 94%. The RF stacking involves 20 cycles which gives a total number of effective turns $\eta_{tot} = 800$. In fact 7 mA ($1.2 \cdot 10^{10}$ ions) of C^{6+} ions with 6.1 MeV/A energy has been measured. The whole process takes about 12 ms.

Figure 17 shows the longitudinal Schottky Spectrum of the RF stack after accumulation of 30 cycles [32].

B. MIMAS Booster — Accumulator for Saturne

MIMAS is a low energy booster — storage ring which accumulates heavy ions from a CRYEBIS (Dione) — RFQ combination at 187 keV/A and accelerates them to 11.9 MeV/A (for $Z/A = 0.5$) for injection in the synchrotron

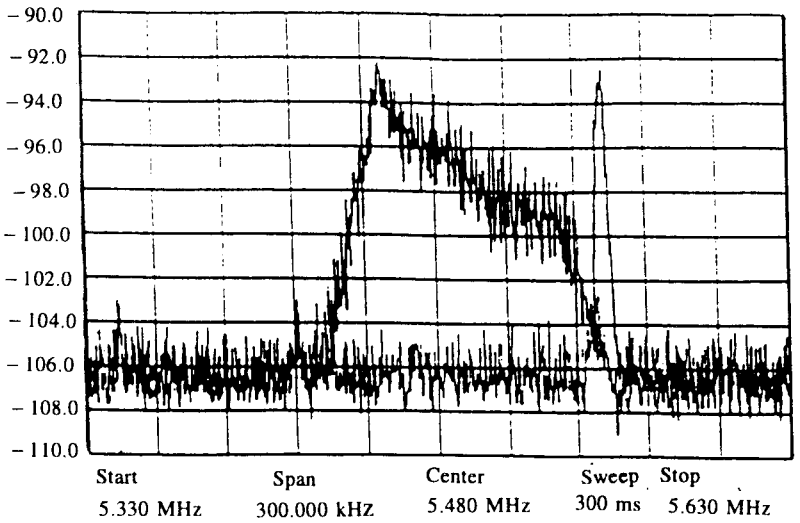

Fig.17. TSR Schottky spectrum of the RF stack after accumulation of 30 cycles [32]

SATURNE [33]. Dione generates ions in short 50 μs pulses at intervals of 20—50 ms.

In MIMAS ions are stacked in the synchrotron phase space by a betatron deceleration scheme [34]. The deceleration voltage up to 500 V is made by flux variation in 8 ion cores installed in one of the straight sections. Up to 8 heavy ions pulses can be injected and stored with a repetition rate of about 100 Hz.

The injection scheme can work with polarized protons and deuterons as well. The pulse produced by the ion source Hyperion is long (1 ms) with constant intensity allowing for a constant filling of MAIMS.

With MIMAS the synchrotron SATURNE is capable of producing beams up to krypton at 700 MeV/A as well as high intensity polarized protons and deuterons at 3 GeV.

4. CHARGE-EXCHANGE INJECTION

Charge exchange injection is now the preferred injection method for proton machines due to its relative simplicity and a very high intensity of stored beams [35,36]. Recently, this injection method has been successfully applied for light ion storage in the CELSIUS [37] and COSY [38] cooler rings.

4.1. Principle of the Charge-Exchange Injection. The principle of charge exchange injection consists in letting an injected beam pass through a thin internal foil [36,63]. Having passed the foil, ions change their charge while energy is practically unaltered and beam rigidity $B\rho$ jumps to a new value according to the relation:

$$B\rho = \frac{A}{300Z}\sqrt{T_n^2 + 2E_{0n}T_n}\,, \tag{4.1.1}$$

where $B\rho$ is in Tm; the kinetic energy T_n per nucleon is in MeV, and the rest of energy per nucleon E_{0n} is also in MeV. This provides a spatial separation for the trajectories of the injected and circulating beams.

The charge exchange process cannot be described by a Hamiltonian. That is why the Liouville theorem for phase space density conservation does not work. This allows us to inject ions many time into one and the same area in the phase space thus increasing the intensity of the stored beam (non-Liouville stacking).

4.2. Equilibrium Charge State Distribution and Equilibrium Thickness of the Stripping Foil. As the beam ions travel through the matter, a relative content of ions in defferent charge states changes. The process is described by the following set of linear differential equations:

$$\frac{d\Phi_k}{dt} = \sum_j \Phi_j \sigma_{jk}\,, \tag{4.2.1}$$

where Φ_j is the percentage of the ions in the j-th charge state in the beam; σ_{jk} is the cross section for the transition $j \to k$; t is the foil thickness in at/cm^2.

The charge state distribution reaches equilibrium for thick enough foils [39,40]. This equilibrium distribution independent of the initial distribution in the beam is determined only by the relations between different charge-exchange cross sections σ_{jk} and the ion velocity. The beam attains charge state distribution equilibrium earlier than a visible particle delay in the foil material is reached. The equilibrium distribution is the solution of the linear system:

$$\sum_j \Phi_j \sigma_{jk} = 0. \tag{4.2.2}$$

So, in order to calculate for the equilibrium distribution and the equilibrium thickness to be calculated, one needs the exact values of electron loss and

capture cross sections σ_{jk}. First theoretical papers on the cross sections in ion-atom collisions have been carried out by N.Bohr. He found for the electron loss [41]:

$$\sigma_e \approx 4\pi a_0^2 \frac{Z_t^2 + Z_t}{q^2} \left(\frac{\beta_1}{\alpha} \right)^{-2}, \tag{4.2.3}$$

where $\alpha = 1/137$ is the fine structure constant and a_0 is the Bohr's radius, and for electron capture (together with Lindhard) [42] we have:

$$\sigma_c = \pi a_0^2 Z_t^{1/3} q^2 \left(\frac{\beta_1}{\alpha} \right)^{-3}. \tag{4.2.4}$$

Unfortunately, the experiments have shown that the above formulae work well only over a quite narrow range of parameters. A lot of semiempirical formulae for electron loss and capture cross sections have been put forward [43—45].

For electron capture the experiments show that:

$$\sigma_c \sim Z_{\text{pr}}^{\alpha 1} V^{\alpha 2} Z_t^{\alpha 3}, \tag{4.2.5}$$

where

$$\alpha_1 = 4 \div 5; \quad \alpha_2 = (2 \div 5); \quad \alpha_3 = 0.15 \div 0.4.$$

The electron loss cross section σ_e increases with target atomic number Z_t and decreases with projectile atomic number Z_{pr}($\sigma_e \sim Z_{\text{pr}}^{\alpha}$, $\alpha = -(1 \div 3)$) and depends strongly on the ion velocity. On the other hand, the experiments show that the cross sections for losses of more than one electron are not negligible. In connection with that there was proposed a semiempirical method [45] for calculations of the cross sections for the loss of one and several electrons by fast multielectron ions. Using this method, which is based on the results of an analysis of experimental data and theoretical calculations, the cross sections ($m = 1$—5) have been obtained for the fast ions of iodine and uranium in nitrogen.

The problem is even more complicated as the case of solid foils strongly differs from that of rare gases. While in rare gases the time between the successive ion-atom collisions is long enough for excited atoms to return to their basic state, in solid foils this time is short and the atom state remains almost unchangeable. This means that all the cross sections should be averaged over

the excited states. For this reason the electron loss cross sections in solids are larger than is gases and the electron capture cross sections are smaller. As a result the equilibrium thicknesses in solid foils are larger (up to ten times) than those in gases [46].

The accelerator experiments [47,48] show that for heavy ions with energies from 3.8 to 10.6 MeV/nucleon the equilibrium thickness of carbon foils lies between 250 to 350 $\mu g/cm^2$.

4.3. Equilibrium Charge State Distributions behind the Stripping Foil. The equilibrium charge state distributions of heavy ion beams on traversing the stripping foil are presented by a Gaussian [49], although the Gaussian describes continuous random variables while the ion charge states q are discrete ones

$$\Phi_q = \frac{1}{\sigma\sqrt{2\pi}} e^{-(q-\bar{q})/2\sigma^2}. \tag{4.3.1}$$

Formula (4.3.1) is valid if the average charge state $\bar{q}$ is not too close to Z_{pr}.

Several empirical formulae have been proposed for the average charge state $\bar{q}$. It is assumed to use the reduced velocity X as an independent variable in all of these formulae:

$$X = \frac{V}{V' Z_{pr}^{0.45}}, \quad V' = 3.6 \cdot 10^8 \text{ cm/s}, \tag{4.3.2}$$

Nikolaev-Dmitriev's formula [50]:

$$\frac{\bar{q}}{Z_{pr}} = (1 + X^{-1/0.6})^{-0.6}, \tag{4.3.3}$$

To-Droin's formula [51]:

$$\frac{\bar{q}}{Z_{pr}} = 1 - e^{-x}, \tag{4.3.4}$$

Shima's formulae [52]:

$$\frac{\bar{q}}{Z_{pr}}(Z_t = 6) = 1 = \exp[-1.25X + 0.32X^2 - 0.11X^3], \tag{4.3.5}$$

$$\frac{\bar{q}}{Z_{pr}}(Z_t \neq 6) = \frac{\bar{q}}{Z_{pr}}(Z_t = 6)[1 + g(Z_t)], \tag{4.3.6}$$

where

$$g(Z_t) = -0.0019(Z_t - 6)\sqrt{X} + 10^{-5}(Z_t - 6)^2 X, \tag{4.3.7}$$

Heckman-Betz's formula [53—55]:

$$\frac{\bar{q}}{Z} = 1 - C\exp\left(-\frac{V}{V_0 Z_{\text{pr}}^{\gamma}}\right), \tag{4.3.8}$$

where C and γ are constants depending on Z_{pr} in the intervals: $C \in (1.07 \div 1.25)$; $\gamma \in (0.57 \div 0.65)$ and $v_0/c = 137$.

Baron-Ricaud's formula [47]:

$$\frac{\bar{q}}{Z} = 1 - C\exp\left(-\frac{83.275\beta}{Z^{0.447}}\right), \tag{4.3.9}$$

where

$$C = \begin{cases} 1, & \text{for } T_{\text{pr}} > 1 \text{ MeV/n}, \\ 0.9 + 0.0769\ T_{\text{pr}}, & \text{for } T_{\text{pr}} < 1 \text{ MeV/n} \end{cases}.$$

Formulae (4.3.1—4.3.5) have been deduced scaling experimental data over an energy range of below 2 MeV/n. Formula (4.3.3) scales the experimental data of wider energy range up to $X = 2.5$ and also describes the cases of non-carbon foils. In [47] the correction for heavier ions ($Z \geq 54$) has been deduced:

$$\bar{q}_p = \bar{q}_p\,[1 - \exp(-12.905 + 0.2124Z - 0.00122Z^2)], \tag{4.3.10}$$

where $\bar{q}_p$ is taken from (4.3.9).

For the standard deviation Nikolaev and Dmitriev [50] propose the following expression:

$$\sigma = 0.5\sqrt{\bar{q}\left(1 - \left(\frac{q}{Z}\right)^{1.67}\right)}. \tag{4.3.11}$$

The correction for heavier ions ($Z \geq 54$) is proposed in [47]:

$$\sigma = \sqrt{\bar{q}_p(0.07535 + 0.19Y - 0.2654Y^2)}\ , \quad Y = \frac{\bar{q}_p}{Z}. \tag{4.3.12}$$

Some experimental data for the charge distribution of Ar ions behind carbon foils of different thicknesses and energy 5.62 MeV/n are presented in Table 3 [47].

Table 3
Ar_{40}^{6+}, $T_n = 5.62$ MeV / n

d, μg/cm²	q				
	14	15	16	17	18
60	1.76	13.69	45.40	32.39	6.74
84	1.26	10.57	39.64	37.86	10.58
120	0.96	8.17	35.11	40.54	14.92
150	0.85	7.95	32.47	42.26	16.78
215	0.55	5.53	26.55	43.79	23.59
300	0.04	3.81	25.10	45.21	25.25

4.4. Heavy Ions Scattering in the Stripping Foil. The Coulomb elastic scattering of beam ions in a stripping foil will cause a change of the trajectory slopes.

The mean energy loss of an ion for unit path length when $m_{pr} \leq 0.2m_t$, where m_{pr} — the particle mass, m_t — the target nucleus mass, is given by [56]:

$$\left(-\frac{dE}{dx}\right)_{0l} = \frac{2\pi Z_{pr}^2 Z_t^2 e^4 n m_{pr}}{m_t E_{pr}} \left\{ \ln \sin \frac{\theta_{min}}{2} + \frac{1}{2} \frac{m_t^2 - m_{pr} m_t - m_{pr}^2}{(m_{pr} + m_t)^2} \right\}. \quad (4.4.1)$$

In (4.4.1) n denotes the number of target atoms in unit volume and E_{pr} — the particle energy.

It can be shown [56] that the ratio of the ionization losses to the Coulomb scattering energy losses is:

$$\frac{\left(-\frac{dE}{dx}\right)_{ion}}{\left(-\frac{dE}{dx}\right)_{sct}} = \frac{1}{\left(\frac{m_0 Z_t}{A_t m_p}\right)} \approx 4000, \quad (4.4.2)$$

where m_p is the proton rest mass and A_t is the atomic weight of the target material.

From (4.4.2) it follows that the energy losses in the Coulomb scattering are negligible.

On the contrary, the particle trajectory changes are very important.

The basic laws of the elastic Coulomb scattering have been well known since the time of Rutherford's pioneer works.

An important role in accelerator practice is played by the multiple scattering in the foil material.

It can be shown that the multiple scattering mean square angle is [56]:

$$\langle\theta^2\rangle = 0.078 \frac{Z_{pr}^2 Z_t^2 t}{E_{pr}^2 A_t} \ln\left\{1.06\cdot10^2 \frac{Z_{pr} Z_t^{1/3}}{\beta_{pr}} \sqrt{\frac{t}{A_t}}\right\}, \tag{4.4.3}$$

where E_{pr} is the particle kinetic energy in MeV and t is the target thickness in g/cm^2.

In [59] the following empirical formula for the multiple scattering mean square angle of heavy ions in solid foils is given:

$$\langle\vartheta^2\rangle = 0.250 \frac{Z_t(Z_t+1)}{A_t} \frac{Z_{pr}^2}{E_{pr}^2} t, \tag{4.4.4}$$

where ϑ is in mrad; stripper thickness t is in μg/cm^2 and particle energy E_{pr} is in MeV.

The average number of scatterings per particle and passage is given by:

$$n_{sct} = 0.0392 \frac{Z_{pr}^2 Z_t^2 \gamma_{pr} t}{A_t E_{pr}^2} \frac{1}{\vartheta_\alpha}, \tag{4.4.5}$$

ϑ_α is the so-called screening angle:

$$\vartheta_\alpha = 4.52\cdot10^{-3} \sqrt{1.78\cdot10^{-4} Z_{pr}^2 Z_t^2 + \beta_{pr}^2} \frac{\sqrt[3]{Z_t}}{E_{pr} \beta_{pr}^2 \gamma_{pr}}, \tag{4.4.6}$$

where t is the target thickness in g/cm^2, E_{pr} is the particle energy in MeV.

4.5. Emittance Growth Due to Elastic Coulomb Scattering in the Stripping Foil. It is convenient to work in the normalized phase space (y, y^*), where y is the transverse coordinate (either X or Z) and

$$y^* = \alpha y + \beta y'. \tag{4.5.1}$$

In (4.5.1) α and β are the Twiss functions and $'$ denotes differentiation with respect to the longitudinal coordinate S.

In the normalized phase space the betatron oscillations can be presented in the form:

$$y = A \cos(\psi + \alpha),$$

$$y^* = A \sin(\psi + \alpha), \tag{4.5.2}$$

where ψ is the betatron phase, $\psi = \int \frac{ds}{\beta(s)}$ and A and α are constants.

Let y and y^* be the Gaussian distributions. The betatron amplitude is:

$$A^2 = y^2 + y^{*2}. \tag{4.5.3}$$

Relation (4.5.3) determines a circle in the normalized phase space with a radius A. In order to find out the amplitude distribution, one has to integrate the joint probability distribution along this circle. In polar coordinates:

$$P(A) = \int_0^{2\pi} p(y,y^*) A d\varphi = \int_0^{2\pi} \frac{A}{2\pi\sigma^2} e^{A^2/2\pi\sigma^2} d\varphi = \frac{A}{\sigma^2} e^{-A^3/2\pi\sigma^2}, \tag{4.5.4}$$

i.e., we have obtained Rayleigh distribution with

$$\sigma^2 = 2\sigma_y^2. \tag{4.5.5}$$

Passing through the stripper the beam particles change by jump the slope of their trajectoty and keep the distance from the equilibrium orbit unchangeable.

$$y = y_0, \quad y^* = y_0^* + \Delta y^* = y_0^* + \beta \Delta y'. \tag{4.5.6}$$

Behind the stripper we have:

$$A^2 = A_0^2 + 2\Delta y^* y_0^* + \Delta y^{*2}. \tag{4.5.7}$$

Averaging (4.5.7) we obtain:

$$\sigma_A^2 = \sigma_{A0}^2 + \sigma_{\Delta y'}^2 = \sigma_{A0}^2 + \beta^2 \sigma_{0\Delta y'}^2 . \tag{4.5.8}$$

The real situation in charge-exchange injection however is more complicated. At the end of the injection process we have on the accelerator circumference simultaneously particles passing N times through the stripper, particles passing $(N-1)$ times and so on up to the particles having crossed the stripper only once.

Obviously, in this case the probability for an amplitude is the normalized sum of probabilities for amplitudes after a definite number of foil crossings:

$$p(A) = \frac{1}{N} \sum_{i=1}^{N} p_i(A). \tag{4.5.9}$$

Then

$$\sigma_A^2 = \frac{1}{N} \sum_{i=1}^{N} \sigma_{Ai}^2 , \tag{4.5.10}$$

but

$$\sigma_{Ai}^2 = \sigma_{A0}^2 + \beta_0^2 \sigma_{\Delta y'}^2 . \tag{4.5.11}$$

Thus, we obtain

$$\sigma_A^2 = \sigma_{A0}^2 + \frac{(N+1)}{2} \beta_0^2 \sigma_{\Delta y'}^2 . \tag{4.5.12}$$

From (4.5.12) we can deduce the emittance growth due to the elastic Coulomb scattering:

$$\varepsilon_N = \frac{\sigma^2 A}{\beta_0} \simeq \varepsilon_0 + \frac{1}{2} N \beta_0 \langle \vartheta^2 \rangle. \tag{4.5.13}$$

4.6. Energy Losses in the Stripping Foil. The energy losses of beam particles in the stripping foil are mainly due to the excitation and ionization of foil atoms.

Mean losses are described by the well-known Bethe-Bloch formula [56—58]:

$$\frac{dE}{dx} = \frac{DZ_t \rho_t}{A_t} \left(\frac{Z_{pr}}{\beta} \right)^2 \left(\ln \left(\frac{2m_e \gamma^2 \beta^2 c^2}{I} \right) - \beta^2 - \frac{\delta}{2} - \frac{e}{Z_t} \right) (1 + \nu), \qquad (4.6.1)$$

where ρ is the mass foil density:

$$D = 4\pi N_A r_e m_e e^2 = 0.3070 \frac{\text{MeV} \cdot \text{cm}^2}{g},$$

and I is the mean ionization potential of medium atoms.

$$I \approx 13.5 Z_t, \text{ eV}, \qquad (4.6.2)$$

δ, c, ν are the phenomenological functions which values are usually negligibly small, δ represents the density effect; and c, shell corrections.

4.7. Emittance Growth Due to the Energy Losses. If the dispersion in the stripper is nonzero, then the energy losses will cause the emittance growth according to the well-known relations:

$$\Delta y = -D_0 \frac{\Delta p}{p},$$

$$\Delta y' = -D_0' \frac{\Delta p}{p}, \qquad (4.7.1)$$

where D_0 and D_0' are the linear and angular dispersions in the stripper and $\Delta p / p$ is related to the energy losses by:

$$\frac{\Delta E}{E} = \beta^2 \frac{\Delta p}{p}, \qquad (4.7.2)$$

where E is the total particle energy.

The minus sign in (4.7.1) implies that traversing the foil the particles remain in the same position while due to the energy losses the corresponding off-momentum orbit jumps to a new position. We will perform our analysis in the normalized phase space (y, y^*), where betatron oscillations are presented by circles. From a simple geometrical analysis one can deduce that:

$$\sqrt{\beta_0 \varepsilon} = \sqrt{\beta_0 \varepsilon_0} + k \sqrt{\Delta y^2 + \Delta y^{*2}}, \qquad (4.7.3)$$

where ε_0 is the initial emittance; ε, a new emittance; and k, the number of turns.

4.8. Ionization Losses Straggling in the Stripping Foil. The maximum energy transferrable by a fast moving charged particle to the electron is [60]:

$$E_{\max} = \frac{2m_e\beta_{pr}^2\gamma_{pr}^2c^2}{1+2\gamma(m_e/m_{pr})+(m_e/m_{pr})^2}. \tag{4.8.1}$$

For our case $E_{\max} = 10.22$ keV.

The ionization losses are statistical in nature. There exists a probability distribution function $f(x, \Delta)$ so that $f(x, \Delta)d\Delta$ is the probability that the ion, on traversing a path length x in the target, will suffer an energy loss between Δ and $\Delta + d\Delta$.

The character of the distribution function depends on the parameter κ [62]:

$$\kappa = \frac{\xi}{E_{\max}}, \tag{4.8.2}$$

where

$$\xi = \frac{2\pi ne^4Z_{pr.eff}^2ZX_t}{m_ev_{pr}^2}, \tag{4.8.3}$$

n is the number of target atoms per unit volume; X, the target thickness; and $Z_{pr.eff}$, the ion effective charge:

$$Z_{eff} = Z\left[1-\exp\left(-0.95\frac{vh}{e^2Z^{2/9}}\right)\right] = Z[1-\exp(-130\beta Z^{-2/9})]. \tag{4.8.4}$$

a) If $\kappa < 0.05$, the distribution is highly asymmetric with respect to a long tail, the so-called Landau's distribution [61]:

$$f(x, \Delta) = \frac{1}{\xi}\varphi(\lambda) \tag{4.8.5}$$

$$\varphi(\lambda) = \frac{1}{2\pi i}\int_{\sigma-i\infty}^{\sigma+i\infty} e^{u\ln u+\lambda u}du$$

$$\lambda = \frac{\Delta - \xi(\ln\frac{\xi}{\xi'}+1-c)}{\xi},$$

where c is Euler's constant $c = 0.5777...$

$$\ln \varepsilon' = \ln \left[\frac{(1-\beta^2) I^2}{mv^2} \right] + \beta^2. \tag{4.8.6}$$

b) If $0.05 < \kappa < 10$, we have the case of the Vavilov's distribution [62]:

$$f(x, \Delta) = \frac{1}{\pi \xi} \kappa \, e^{\kappa(1+\beta^2 c)} \int_0^\infty e^{\kappa f_1} \cos(y f_1 + \kappa f_2) dy, \tag{4.8.7}$$

$$f_1 = \beta^2 (\ln y - Ci(y)) - \cos y - y \, Si(y),$$

$$f_2 = y(\ln y - Ci(y)) + \sin y + \beta^2 Si(y),$$

where Si and Ci are the sin and cos integrals.

c) If $\kappa > 10$, the distribution is Gaussian:

$$f(x, \Delta) = \frac{1}{\sqrt{2\pi \gamma x}} e^{-\frac{(\Delta - \alpha x)^2}{2\gamma x}}, \tag{4.8.8}$$

where according to the Landau's notation

$$\alpha \equiv \langle \Delta \rangle = \int_0^\infty \varepsilon w(\varepsilon) d\varepsilon \tag{4.8.9}$$

and

$$\gamma = \int_0^{\varepsilon_{max}} \varepsilon^2 w(\varepsilon) d\varepsilon = \frac{\xi}{x} \varepsilon_{max} \left(1 - \frac{1}{2} \beta^2 \right) \tag{4.8.10}$$

are the mean and variance for unit path length.

The situation with charge exchange injection is a little bit more complicated because we have simultaneously on the orbit particles traversing the foil N-times, $(N-1)$ times up to one time. Then the common probability density is:

$$p(\Delta) = \frac{1}{N} \sum_{i=1}^{N} p_i(\Delta), \tag{4.8.11}$$

where $p_i(\Delta)$ is the probability density for particles traversing the foil i-th times.

From (4.8.11) and taking into account the large value of N, one can deduce for the energy dispersion in a stored beam:

$$\sigma_N^2 = \sigma_0^2 + \frac{N}{2}\sigma_t^2 + \frac{N^2}{12}\langle\Delta\rangle_t^2, \tag{4.8.12}$$

where σ_0^2 is the energy dispersion in the incident beam, σ_t^2 is the dispersion of ionization losses in the foil material (one passage through the target) and $\langle\Delta\rangle_t$ are mean ionization losses in the foil.

4.9. Ion Storage-Fixed Orbit Bump Mode. In this mode the orbit bump remains unchangeable. Ions pass through the stripper many times until an equilibrium is attained or until other limited factors — scattering and energy losses — begin to restrict the number of stored particles.

The storage process can be described in the following way.

a) During the first turn the number of stored particles will increase as $N_t = \Delta I t$, where $\Delta I = I_0\sigma_1 nt$ is the ion current behind the target; I_0, the injected beam current; σ_1, the circulating charge ($Z_c \approx q$) formation cross section; n, the number of target atoms per unit volume; and t, the target thickness. At the end of the first turn we will have $N_t = \Delta I.T$ particles on the orbit, T being the period of the synchronous particle.

b) During the second turn the circulating particles will pass through the target for the second time. Let σ_2 be the circulating charge formation cross section for the circulating particles. Generally speaking, $\sigma_2 \neq \sigma_1$ as the charge state distribution in the injected beam differs from that in the circulating beam. If the former is centered on charge number $Z_0 \neq Z_c$ (otherwise charge-exchange injection will not work) the circulating beam contains only ions in one charge state. Ions in other charge states have been already lost on the walls of the vacuum chamber because for them $\Delta Z/Z_c$ is quite large. Simultaneously new particles are injected into the ring, and these particles will pass through the stripping foil only once. Summarizing, we can obtain for the number of the stored particles:

$$N_t = \Delta I(t - T) + \sigma_2 nt\Delta I(t - T) + \Delta I(2T - t) \tag{4.9.1}$$

and at the end of the second turn:

$$N_{2T} = \Delta I(1 + \sigma_2 nt)T. \tag{4.9.2}$$

Following this way of reasoning, we can obtain for the k-th turn $N_t = \Delta I(1 + b + \ldots + b^{k-1})T$, where $b = \sigma_2 nt$. Summing geometrical progression in the brackets, we get:

$$N_k = N_\infty(1 - b^k), \tag{4.9.3}$$

where

$$N_\infty = \left(\frac{a}{1-b}\right) I_0 T, \quad a = \sigma_1 nt, \quad b = \sigma_2 nt, \tag{4.9.4}$$

T is the period of the synchronous particle; I_0 being the injected current; σ_1, the cross section for the formation of ions with equilibrium charge from the injected ions; and σ_2, the cross section for the formation of ions with equilibrium charge from the circulating ions.

In the specific case of stripping target with equilibrium thickness, the charge state distribution behind the target will reach equilibrium which means that it is independent of the charge distribution in the incident beam and that it will be no longer changed. For the target of equilibrium thickness $\sigma_1 nt = \sigma_2 nt = \Phi_{zc}$, i.e., the probability of circulating charge formation for the injected beam is equal to that for the circulating beam. Formula 4.9.4 becomes simpler:

$$N_k = N_\infty(1 - \Phi_{zc}^k) \tag{4.9.5}$$

$$N_\infty = \left(\frac{k}{1 - \Phi_{zc}}\right) I_0 T. \tag{4.9.6}$$

4.10. Ion Storage — Moving Orbit Bump Mode. In this mode the orbit bump gradually reduces to zero during the injection.

When the orbit is close to the centre of the stripper, the injected particles will cross it every turn. On the contrary, the particles injected when the orbit lies outside the stripper will undergo betatron oscillations and will avoid the stripper most of the turns. In other words, we have a kind of combination between the multiturn and the stripping injections. Such a combination allows the number of the injection turns to be increased many times.

The goal of this section is to assess the total number of injected particles in the mode under consideration. We will use a beam model with a uniform charge distribution and clear-cut boundaries which are circles in the normalized phase

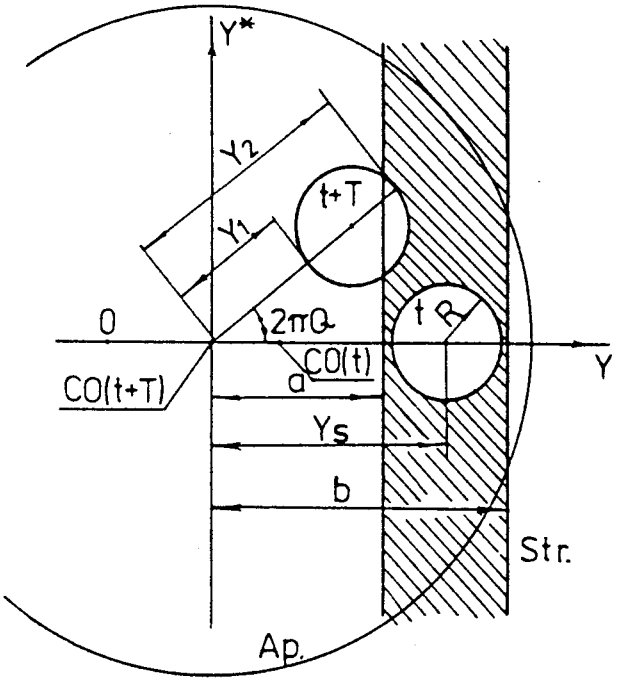

Fig.18. Charge exchange injection with a moving orbit bump

space. Let us take a beam slice $dN = I_0 dt$ injected at time t (Fig.18). After one turn the slice will occupy the position forming angle $\alpha = 2\pi Q$ with the initial position as is depicted in Fig.18.

Let us denote the beam radius by $R = \sqrt{\beta_0 \varepsilon}$ and the aperture radius by A. As $A >> R$, we will approximate here the aperture boundary lying within the slice confines with a straight line, so the part of the slice outside the aperture will be approximated with a circle segment.

Under the above assumptions a pure geometrical analysis can be carried out. From Fig.1 we obtain that:

$$y_1(t) = y_s - R - y_{c0}(t),$$

$$y_2(t) = y_s + R - y_{c0}(t). \tag{4.10.1}$$

For the utmost left y' and utmost right y'' projection of the slice on the y axis we have:

$$y'(t+jT) = y_{c0}(t+jT) + y_1 \cos j\,2\pi Q - R(1-\cos j\,2\pi Q)$$

$$y''(t+jT) = y_{c0}(t+jT) + y_2 \cos j\,2\pi Q + R(1-\cos j\,2\pi Q)$$

$$j = 0,1,2, \ldots . \tag{4.10.2}$$

The stripper edge cuts a circle segment with an area S_1 from the beam slice. If H is the edge distance to the slice center we can write:

$$H(t+jT) = a - y_{c0}(t+jT) - (y_s - y_{c)}(t)) \cos j\,2\pi Q \tag{4.10.3}$$

and

$$S_1(t+jT) = R^2 \arccos\left(\frac{H}{R}\right) - H\sqrt{R^2 - H^2} \quad j = 0,12, \ldots . \tag{4.10.4}$$

Another kind of restriction comes from the machine aperture. The aperture is centered on the instantaneous closed orbit position. This means that at the beginning of injection, when the orbit bump passes through the stripper we will have no aperture limitations. However, when the orbit bump is small enough to go close to the machine centre, considerable aperture restrictions on the beam will take place. The closer the orbit passes to the machine centre the stronger aperture restrictions will be.

As mentioned above, we will consider that the aperture cuts also a circle segment (with an area S_c) from the beam slice. This approximation is as much better as A is bigger than R. Similar to (4.10.4) we can deduce that

$$S_c^2(t) = R \arccos\left(\frac{H_c}{R}\right) - H_c\sqrt{R^2 - H_c^2}\,, \tag{4.10.5}$$

where

$$H_c(t) = y_{c0}(t) + A - y_s \tag{4.10.6}$$

is the distance between the aperture edge and the slice centre.

The main parameter of our analysis is the transition coefficient k — the percentage of particles having passed through the stripper and accepted in the aperture.

It can be shown that

$$k(t+jT) =$$

$$= \begin{cases} \Phi, \quad a < y'(t+jT), \quad R \le H_0(t) \\ \dfrac{\pi R - S_c(t)}{\pi R^2}\Phi, \quad a \le y'(t+jT), \quad H_c(t) < R \\ \dfrac{\pi R^2 - (1-\Phi)S_1(t+jT)}{\pi R^2}, \quad y'(t+jT) < a < y''(t+jT), \quad H_c(t) \ge R \\ \dfrac{\pi R^2 - (1-\Phi)S_1(t+jT) - \Phi S_c(t)}{\pi R^2}, \quad y'(t+jT) < a < y''(t+jT), \quad H_c(t) \ge H(t+jT) \\ \dfrac{\pi R^2 - S_c(t)}{\pi R^2}, \quad y'(T+jT) < a < y''(t+jT), \quad H_c(t) < H(t+jT) \\ 1, \quad y''(t+jT) < a, \quad H_c(t) \ge R \\ \dfrac{\pi R^2 - S_c(t)}{\pi R^2}, \quad y''(t+jT) < a, \quad H_c(t) < R \end{cases} \tag{4.10.7}$$

$$j = 0,1,2, \ldots$$

where

$$\Phi = \begin{cases} \sigma_1 nt, & \text{for the injected beam} \\ \sigma_2 nt, & \text{for the circulating beam} \end{cases} \tag{4.10.8}$$

is the probability for the formation of ions with equilibrium charge.

Let us consider the case of an exponential law of orbit motion:

$$y_{c0}(t) = y_s \, e^{-t/\tau}. \tag{4.10.9}$$

Let r be the number of turns during which the orbit moves from the centre of the stripper to the center of the machine.

Let us describe the particle storage turn by turn. During the very first turn:

$$N_1 = \int_0^T \prod_{j=0}^{r} k(t+jT) I_0 dt \tag{4.10.10}$$

particles will be stored in the ring. Multiplication from 0 to r in (4.10.10) describes successive crossing of the target while integration describes continuous orbit motion. During the second turn the number of stored particles increases to:

$$N_2 = N_1 + \int_T^{2T} \prod_{j=0}^{r-1} k(t+jT) I_0 dt. \tag{4.10.11}$$

Generating, we arrive at the following expression for the total number of stored particles

$$N = \sum_{i=0}^{r} \left\{ \int_{iT}^{(i+1)T} \prod_{j=0}^{r-1} k(t+jT) I_0 dt \right\}. \tag{4.10.12}$$

4.11. Charge-Exchange Injection into Nuclotron Booster. As an example we will give in this paper the simulations of the charge-exchange injection into Nuclotron booster [63].

The main booster parameters have been given in paragraph 2. Some additional parameters important for the injection process are: injection energy for protons — 20 MeV and for ions with $Z/A = 0.5$ — 5 MeV/n; beam rigidity at injection — 0.647 Tm; injector emittance — 40π mm · mrad; booster acceptance —260π mm.mrad; momentum spread at injection — $\pm 2.10^{-3}$.

Some results of the simulation follow.

Figure 19 depicts the mean square angle for multiple scattering in the carbon stripping target.

The calculated emittance growth is plotted in Fig.20.

The energy losses for the test ions are plotted in Fig.21.

The calculated values of the parameter χ are: 15 for Ar_{40}^{14+}, 1.9 for C_{12}^{5+} and 0.3 for Li_6^{2+}. This means that the probability distribution of the ionization losses is normal for heavier ions while it is Vavilov's one for light ions. Thus, the standard deviation for Ar_{40}^{14+} and a 100 $\mu g/cm^2$ thickness of the target is $\sqrt{\gamma\varkappa} = 39.1$ keV. The calculated standard deviation is 17 keV for C_{12}^{5+} and 5 keV for Li_6^{2+}.

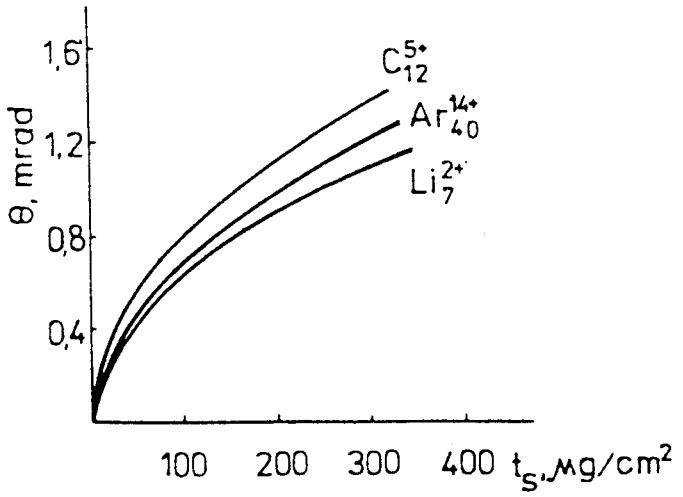

Fig.19. Multiple scattering rms angle for charge-exchange injection into Nuclotron booster [63]

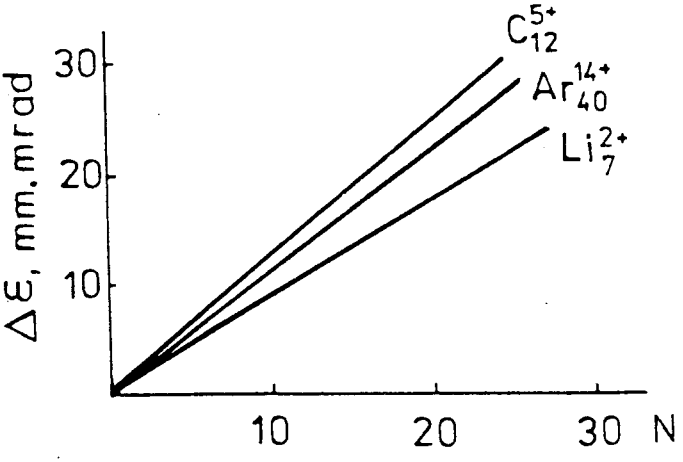

Fig.20. Emittance growth in the Nuclotron booster due to multiple scattering; the target thickness 100 μg/cm², $\beta_0 = 4.5$ m [63]

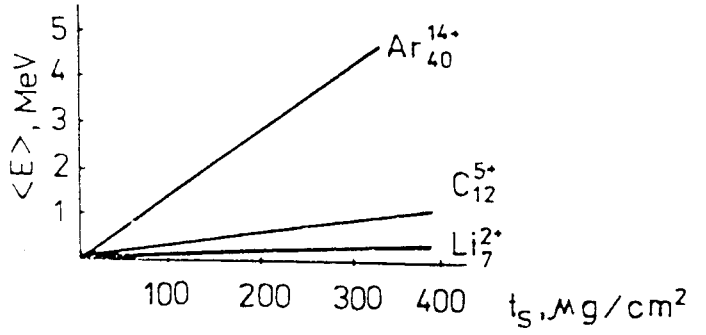

Fig.21. Energy losses in the Nuclotron booster carbon stripping foil [63]

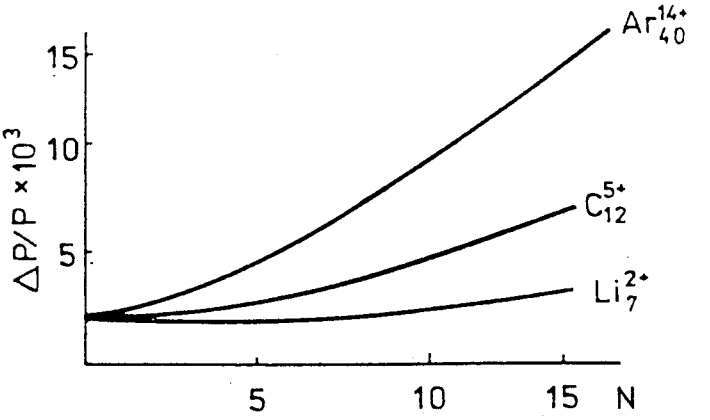

Fig.22. Additional momentum spread in the Nuclotron booster due to the ionization losses in the stripping target [63]

The additional momentum spread due to the ionization losses is given in Fig.22.

The ion storage is shown in Fig.23.

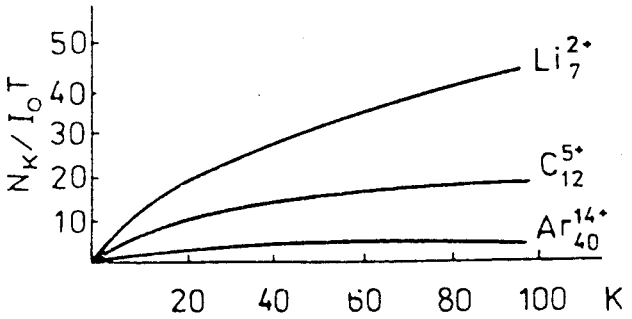

Fig.23. Ion storage in the Nuclotron booster for charge exchange injection with fixed orbit bump [63]

REFERENCES

1. **Rees G.H.** — CERN Accel. School, Geneva, 1994, p.731.
2. **Einckhoff H. et al.** — 1st EPAC, Rome, 1988.
3. **Reinstad D.** — 2nd EPAC, Nice, 1990, p.128.
4. **Barton M.Q.** — BNL Preprint, BNL-AADD-57, 1964.
5. **Fenster S. et al.** — IEEE Trans. Nucl. Sci., 1976, vol.NS-28, p.2574.
6. **Claus J. et al.** — IEEE Trans. Nucl. Sci., 1973, v.NS-30, p.342.
7. **Schindl K., Van der Stok P.** — CERN Preprint, MPS/BR Int./74-2, 1974.
8. **Van der Stok P.** — CERN Preprint, PS/OP/Int.76-1, 1976.
9. **Van der Stok P.** — CERN Preprint, PS/OP/Int.77-12, 1977.
10. **Bovet C., Lamotte D.** — CERN Preprint, SI/Int. DL/69-13, 1969.
11. **Angelov V., Dinev D.** — Bulg. J. Phys., 1996, No.4, p.56.
12. **Issinsky I.B., Mikhailov V.A.** — JINR Preprint, P1-91-2, Dubna, 1991.
13. **Dinev D.** — Bulg. J. Phys., 1993, v.20, No.3/4, p.25.
14. **Titov V.A., Schukeilo I.A.** — J. Tech. Phys., 1968, v.38, p.1752.
15. **Gromov A.M., Cherenkov P.A.** — 13 Allunion Part. Accel. Conf. M. 1973, p.110.
16. **Bryant P.J.** — CERN Accel. School, 1989, p.50.
17. **Roser T.** — 4th EPAC, London, 1994, p.151.
18. **Blasche K., Franzke B.** — 4th EPAC, London, 1994, p.133.
19. **Abrahamson K. et al.** — 4th EPAC, London, 1994, p.380.
20. **Symon K., Sessler A.** — CERN Symp. High En. Accel. 1956, v.1, p.44.

21. **Bruckner A. et al.** — NIM, 1970, v.77, p.78.
22. **Ciapala E.** — CERN Accel. School, 1984, v.1, p.195.
23. **Montague D.W.** — 1st Int. School Part. Accel., «Etore Mayorana» Center, 1976.
24. **Bruck H.** — Accelerateurs circulaires de particules. Paris, Press Universitaires, 1966.
25. **Le Duff J.** — CERN Accel. School, 1984, v.1.
26. **Lichtenberg A.J.** — Phase-Space Dynamics of Particles, NY, John Willey Inc..
27. **Lebedev A.N.** — Sov. At. Ener., 1960, v.9, p.189.
28. **Symon K. et al.** — Int. Conf. High Ener. Accel. Geneva, 1959, v.1, p.58.
29. **de Jonge M.J., Messerschmidt E.W.** — IEEE Trans. Nucl. Sci., 1973, v.NS-20, p.796.
30. **Bisoffi G.** — Ph. D. Thesis, Heidelberg Universität, 1989.
31. **Jaeschke E. et al.** — 1st EPAC, Rome, 1988.
32. **Bisoffi G. et al.** — NIM, 1990, v.A287, p.320.
33. **Chamonard P.A. et al.** — 2nd EPAC, Nice, 1990.
34. **Ciret J.C.** — SATURNE Preprint, LNS-SD/MIMAS 88-02, 1988.
35. **Dimov G.I.** — INP Novosibirsk Preprint, 304, 1969.
36. **Simpson J.D.** — IEEE Trans. Nucl. Sci., 1973, v.NS-20, p.198.
37. **Hedblom K. et al.** — 3rd EPAC, Berlin, 1992.
38. **Martin S. et al.** — NIM, 1985, v.A236, p.249.
39. **Nikolaev V.S.** — JINR Part. Accel. School, 1985.
40. **Dmitriev I.S. et al.** — NIM, 1986, v.B14, p.515.
41. **Bohr N.** — Danske Mat. Fys. Medd., 1948, v.18, No.8.
42. **Bohr N., Lindhard J.** — Danske Mat. Fys. Medd., 1954, v.28, No.7.
43. **Kozlov S.I.** — JINR Preprint, 9-83-268, Dubna, 1983.
44. **Franzke B.** — CERN Accel. School, 1992, p.100.
45. **Alonso J. et al.** — IEEE Trans. Nucl. Sci., 1979, p.1.
46. **Zaikov V.P. et al.** — NIM, 1984, v.B5, p.10.
47. **Baron E. et al.** — NIM, 1993, v.A328, p.177.
48. **Clark R.B. et al.** — NIM, 1990, v.A133, p.17.
49. **Xuan K.J., Droin R.** — NIM, 1979, v.160, p.461.
50. **Nikolaev V.S., Dmitriev I.S.** — Phys. Lett., 1968, v.284, p.277.
51. **To K.X., Droin R.** — NIM, 1979, v.160, p.461.
52. **Shima K. et al.** — NIM, 1982, v.200, p.605.
53. **Heckman H.H. et al.** — Phys. Rev., 1962, v.129, p.1240.
54. **Betz H.D. et al.** — Phys. Lett., 1966, v.22, p.64.
55. **Betz H.D.** — Rev. Mod. Phys., 1972, v.44, p.465.
56. **Abramov A.I., Kazanskii J.A., Matusevich E.C.** — Experimental Methods of Nuclear Physics, M, Atomizdat, 1970.

57. **Chirkov Y.M., Yudin N.P.** — Nuclear Physics, M. Nauka, 1974.
58. **Muchin K.P.** — Experimental Nuclear Physics, M., Nauka, 1974.
59. **Joy T.** — NIM, 1973, v.A106, p.237.
60. **Particle Data Group.** — Phys. Lett., 1986, v.170B, No.1.
61. **Landau L.D.** — Selected papers, M., v.1, 1969, p.482.
62. **Vavilov P.V.** — JETP, 1957, v.32, p.920.
63. **Angelov V. et al.** — JINR Preprint, E9-94-369, Dubna, 1994.